

# Tunnel ionization of deep impurities by far-infrared radiation

S D Ganichev<sup>†,‡</sup>, I N Yassievich<sup>‡</sup> and W Prettl<sup>†</sup>

<sup>†</sup> Institut für Angewandte Physik, Universität Regensburg, 93040 Regensburg, Germany

<sup>‡</sup> A F Ioffe Physicotechnical Institute, Russian Academy of the Sciences, St Petersburg, 194021, Russia

Received 13 November 1995, accepted for publication 13 February 1996

**Abstract.** Tunnel ionization of semiconductor deep impurity centres has been investigated in a field of far-infrared radiation where photon energies are several factors of ten smaller than the binding energy of the impurities. Depending on the radiation electric field strength, ionization is caused by phonon-assisted tunnel ionization or direct electron tunnelling. Applying high-power pulsed lasers, two types of impurities have been studied: substitutional on-site acceptors in Ge and autolocalized  $DX^-$  centres in  $Al_xGa_{1-x}Sb$ . The experimental results are analysed in terms of the theory of multiphonon and cold carrier emission of deep impurities in the adiabatic approximation. Tunnelling times have been measured for both types of impurities. Due to different tunnelling trajectories of on-site and autolocalized centres, the tunnelling time is in the first case larger and in the other case smaller than the reciprocal temperature multiplied by universal constants. This allows us to distinguish in a direct way between the two types of configuration potentials of impurities. The results demonstrate that high-frequency far-infrared laser pulses may be used to study the elementary process of tunnelling in extremely large electric field strengths, avoiding contact phenomena and avalanche breakdown.

## 1. Introduction

Deep centres in semiconductors have been the subject of extensive studies [1–5]. They are essential in the control of the electronic properties of semiconductor materials. Deep impurities can reduce the conductivity by trapping carriers or compensating shallow impurities and can act as non-radiative recombination centres, reducing the lifetime of free carriers. One of the aspects of investigations of deep impurities is the effect of an electric field on the thermal emission and capture of carriers. Emission and capture are of great importance for the kinetics and dynamics of semiconductors and for the investigation of electron–phonon interaction of deep centres. In particular, ionization or capture in an electric field are practically the only methods of finding the parameters of multiphonon transitions which govern non-radiative processes associated with deep defects. The electric field stimulation of ionization and capture has been extensively studied by applying static electric fields (e.g. deep-level transient spectroscopy (DLTS), impact ionization etc). Recently, the ionization of semiconductor deep impurity centres has been observed by applying far-infrared radiation with photon energies several factors of ten smaller than the binding energy of the impurities. Preliminary results for Au and Hg impurities in Ge and  $DX^-$  centres in  $Al_xGa_{1-x}Sb$  have been published in [6–9]. It has been shown that the ionization is caused by tunnelling processes in the electric field of

the high-power radiation. This observation gives a new method of investigating semiconductor properties based on the effect of high electric fields. Applying high static electric fields usually runs into difficulties because of field inhomogeneities in the sample due to contact potentials. The method described here utilizes the electric field of far-infrared radiation with frequencies in the terahertz range. The application of high-power lasers emitting short pulses is free of such problems and allows us to work with substantially higher electric field strengths than in the d.c. case without driving the material into avalanche breakdown instabilities or destroying the sample.

In this paper we present experimental results of terahertz tunnelling ionization of different types of deep impurities and give a detailed comparison with theory. The measurements have been carried out over a wide range of electric fields and temperatures which allows us to identify the elementary process of carrier emission caused by the high-frequency electric field. The emission probability has been determined by recording the photoconductive signal in response to short laser pulses at photon energies much smaller than the binding energy of the impurities. As a main result phonon-assisted tunnelling ionization of impurities has been observed in a wide range of electric field strengths and temperatures. For charged impurities like the deep acceptors in Ge, at relatively low electric field an enhancement of ionization has been found due to the Poole–Frenkel effect. At very high fields, on the

other hand, the photoconductive signal is determined by direct tunnelling of carriers out of the impurity ground state without involving thermal phonons.

The paper is organized as follows. In section 2 we describe the experimental set-up and show some basic results. Section 3 briefly reviews the theory of tunnel ionization of deep impurities in an electric field. In section 4 we present the experimental data and analyse the results with respect to the theory. From the observed electric field dependence of the emission rates we determine tunnelling times as a function of the temperature. It is shown that the magnitude of the tunnelling time allows us to draw conclusions about the configuration of the adiabatic potentials of the deep impurities. In section 5 we summarize this work.

## 2. Experimental set-up and basic results

The investigation of terahertz tunnel ionization has been carried out on two different types of deep impurity centres: on-site substitutional impurities and autolocalized  $DX^-$  centres.

On-site impurities have been investigated in p-type Ge doped with Au, Hg, Cu and Zn as deep acceptors having thermal binding energies of  $\varepsilon_T \sim 150$  meV, 90 meV, 40 meV and 30 meV respectively [5]. The acceptor density of the samples was in the range  $10^{14}$ – $10^{15}$   $\text{cm}^{-3}$ . All the impurities in the investigated samples were singly charged. This fact will be important for small far-infrared intensities where the Poole–Frenkel effect has been observed.

The  $DX^-$  centres have been investigated in  $\text{Al}_x\text{Ga}_{1-x}\text{Sb}$  doped with tellurium resulting in n-type conduction ( $n = 4 \times 10^{17}$   $\text{cm}^{-3}$ ). All the essential features of the  $DX^-$  centres, in particular persistent photoconductivity, have been observed. The compositions of the samples used here are  $x = 0.28$  and  $0.5$ . More details of the properties of these samples can be found in references [10–12].

The ionization of impurities due to high-power pulsed far-infrared radiation has been measured by the usual method of detecting photoconductivity. The change of the conductance of bulk semiconductor samples upon irradiation has been recorded for single laser pulses with a digital oscilloscope. The radiation source was a high-power pulsed far-infrared molecular laser optically pumped by a TEA  $\text{CO}_2$  laser. Using  $\text{NH}_3$  and  $\text{CH}_3\text{F}$  as active laser gases, 40 ns pulses with a peak power of 50 kW have been obtained at wavelengths,  $\lambda$ , of 90.5  $\mu\text{m}$ , 152  $\mu\text{m}$  and 250  $\mu\text{m}$ . The photon energies corresponding to these wavelengths are 13.7 meV, 8.2 meV and 5 meV respectively. In all cases the energy of the quanta has been substantially smaller than the ionization energies of the impurities.

The samples were placed in a variable temperature optical cryostat. Measurements have been carried out in the temperature range 4.2–100 K where in thermal equilibrium practically all charge carriers are bound to the impurity ground states. A series of cold and warm black polyethylene (1 mm thick), Teflon and crystal quartz windows were used to transmit far-infrared radiation while rejecting near-infrared and visible light.

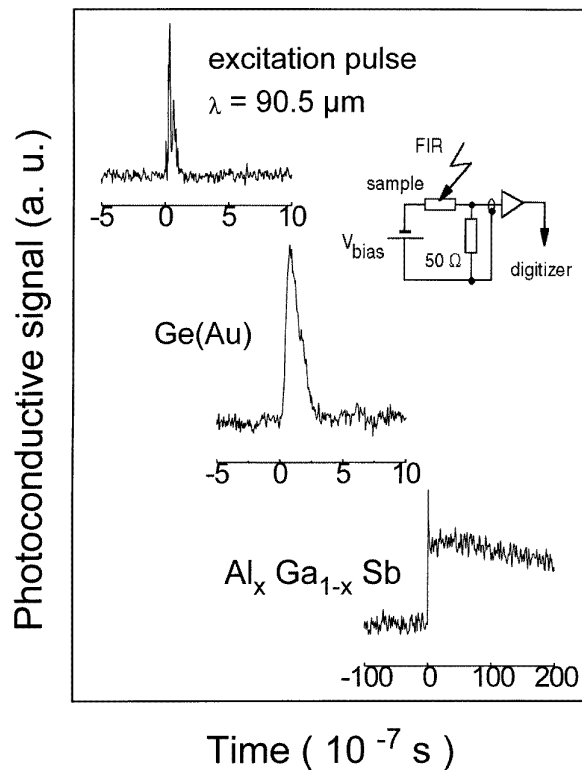


**Figure 1.** Oscilloscope recordings of the excitation pulse and photoconductivity of Ge(Au) and  $\text{Al}_x\text{Ga}_{1-x}\text{Sb}$  for  $\lambda = 90.5$   $\mu\text{m}$  obtained at  $T = 77$  K.

The photoconductivity measurements have been carried out using a standard 50  $\Omega$  load resistor circuit, taking care that the bias voltage across the sample was substantially below the threshold of electric breakdown, which is at about  $5$   $\text{V cm}^{-1}$ . The experimental set-up is shown schematically in the inset of figure 1. The irradiation of the samples with far-infrared pulses leads to a change of conductivity. A photoconductive response, rising superlinearly with the incident radiation power, could be observed in all samples and at all used wavelengths in spite of the fact that the photon energy of the exciting radiation is several factors of ten less than the thermal ionization energy of the impurities,  $\varepsilon_T$ . The sign of the photoconductive signal corresponds to a decrease in sample resistance and thus to an increase of the free carrier concentration. The decay time of the response is different for different types of impurities. Figure 1 shows typical pulse shapes for both types of impurities. For deep on-site impurities in Ge the time constant is somewhat longer than the laser pulse. The decay time of the signal (at  $T = 77$  K it is 50 ns for Ge(Hg) and 80 ns for Ge(Au), see figure 1) represents the lifetime of the excited carriers [13, 14]. In the case of autolocalized  $DX^-$  centres in  $\text{Al}_x\text{Ga}_{1-x}\text{Sb}$ , the signals consist of two components (see figure 1), a fast one with decay time of about 80 ns and a long tail which does not decay within the presented timescale of figure 1. Measurements of the radiation-induced conductivity change of the sample by a d.c. voltmeter have shown that this part of the signal persists for several hundreds of seconds, which corresponds to the

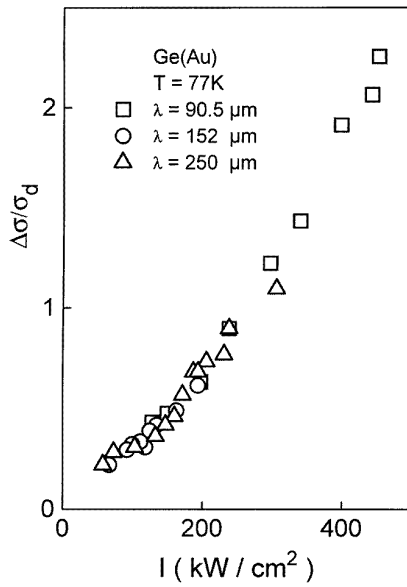


**Figure 2.** Photoconductivity signal  $\Delta\sigma/\sigma_d$  of Au-doped p-Ge (binding energy  $E_i \sim 150$  meV) at  $T = 77$  K as a function of intensity for three wavelengths,  $\lambda$ :  $90.5\ \mu\text{m}$  (photon energy 13.7 meV,  $\square$ ),  $152\ \mu\text{m}$  (8.2 meV,  $\circ$ ) and  $250\ \mu\text{m}$  (5 meV,  $\triangle$ ).

lifetime of persistent photoconductivity observed for  $\text{DX}^-$  centres in the investigated sample [12]. The observation of a positive persistent photoconductivity shows that this signal is caused by the detachment of electrons from  $\text{DX}^-$  centres. The fast component of the signal can be attributed to ionization of native Ga acceptors [15] or intraband  $\mu$ -photoconductivity due to electron heating. This signal component is not of interest for the present investigation. Because of the large difference of the decay times, the signals may easily be distinguished. All further data will be related just to the slow, persistent photoconductivity component of the signal.

The sign of the photoconductive signal and its decay time corresponding to the lifetime of excited carriers demonstrate that photoionization of deep impurities by light with  $\hbar\omega \ll \varepsilon_T$  takes place. Therefore other mechanisms such as free carrier heating or optical rectification can be ruled out. In particular, the persistent change of the conductivity in the case of  $\text{DX}^-$  centres clearly proves ionization of the deep impurities. In figure 2 the photoconductive signal of Ge doped with Au ( $\varepsilon_T \sim 150$  meV) at  $T = 77$  K is shown as a function of radiation intensity for three different wavelengths. Figure 3 shows the data for another deep on-site impurity (Hg in Ge) for two different wavelengths displayed in a log-linear plot. The conductivities at irradiation and in the dark are denoted by  $\sigma_i$  and  $\sigma_d$ , respectively. Because the duration of the excitation pulses is shorter than the capture time of non-equilibrium carriers, recombination may be ignored during the excitation. Therefore the experimentally determined relative change in conductivity,  $\Delta\sigma/\sigma_d = (\sigma_i - \sigma_d)/\sigma_d$ , corresponds to the relative change of free carrier density, which is proportional to the ionization probability of the impurities.

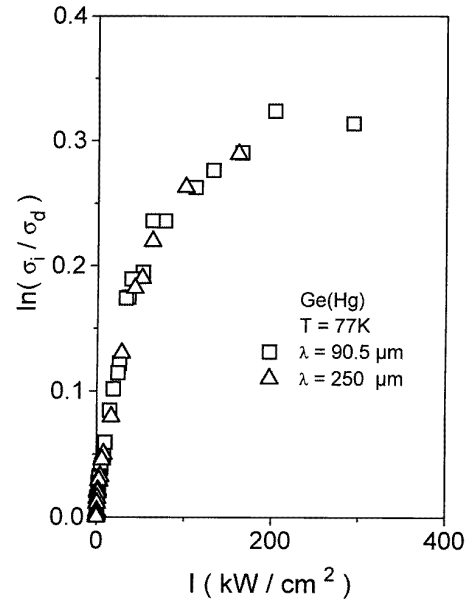


**Figure 3.** Dependence of  $\ln(\sigma_i/\sigma_d)$  for Ge(Hg) ( $E_i \sim 90$  meV) at 77 K on intensity  $I$  for two wavelengths,  $90.5\ \mu\text{m}$  (13.7 meV,  $\square$ ) and  $250\ \mu\text{m}$  (5 meV,  $\triangle$ ).

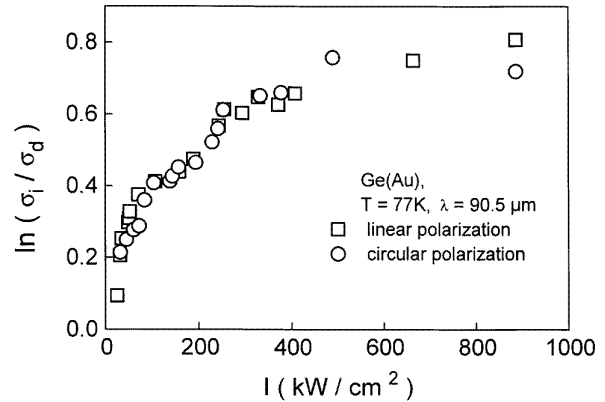


**Figure 4.** Dependence of  $\ln(\sigma_i/\sigma_d)$  for Ge(Au) ( $E_i \sim 150$  meV) at 77 K on intensity  $I$  at  $\lambda = 90.5\ \mu\text{m}$  for linearly ( $\square$ ) and circularly ( $\circ$ ) polarized radiation.

The measurements showed that for a given sample the strength of the photoconductive signal as a function of intensity is the same for all used wavelengths in the whole range of available laser power. Thus, the probability of optical excess carrier generation is independent of the photon energy in the present spectral range. This is demonstrated in figures 2 and 3 which show that the curves for all wavelengths coincide within the accuracy of the measurement. The signal is also independent of the polarization of radiation. This is demonstrated in figure 4 where the photoconductive signal of Ge(Au) as a function of intensity is shown for linearly and circularly polarized radiation at  $\lambda = 90.5\ \mu\text{m}$ .

The photoionization of deep impurities by light with  $\hbar\omega \ll \varepsilon_T$  and the strong nonlinear dependence on intensity of this process may generally be associated with several mechanisms of non-equilibrium carrier generation

such as multiphoton ionization [16, 17], photon-assisted tunnel ionization [18], light impact ionization [19], and phonon-assisted [5, 20, 22] or direct tunnelling [5, 22] in the electric field of the radiation. All these processes show a distinct dependence on irradiation frequency. Increasing the radiation frequency raises the generation rate of non-equilibrium electrons as a result of multiphoton absorption and photon-assisted tunnelling, whereas the rate decreases in the case of light impact ionization. In contrast, tunnel ionization in the field of an optical wave is expected to be independent of frequency as long as the radiation frequency is substantially smaller than the vibration frequency of the impurity. The observed frequency independence of the signal in figures 2 and 3 allows us to conclude that the free carrier generation is due to tunnelling [6–9]. In this case the generation rate is determined by the strength of the electric field of the radiation and not by the number of quanta. Thus, other nonlinear optical mechanisms can be ruled out.

### 3. Ionization of deep impurities in an electric field

#### 3.1. Adiabatic approximation

The binding energy of deep centres is much larger than the average phonon energy and therefore thermal emission may only be achieved by multiphonon processes. As long as the adiabatic approximation holds, the electron–phonon interaction can be treated in the semi-classical model of adiabatic potentials. In most cases deep impurities have one bound state which phenomenologically may be attributed to a spherical steep and narrow potential well. The depth of the potential well sensitively depends on the distance of the impurity and the neighbouring atoms. Thus, lattice vibrations involving these atoms modulate the energy level of the impurity bound state [21] as sketched in figure 5. In the course of thermal vibrations the bound state level may eventually come up to the level of the continuous spectrum, enabling the electron to move from the localized state into the corresponding band [21]. To describe this behaviour a one-mode model with a single configuration coordinate  $x$  is assumed. This approximation is justified because the breathing mode of local vibrations is most effective in multiphonon ionization of deep impurities. In figure 6 two basically different potential diagrams are shown representing a substitutional on-site impurity of weak electron–phonon coupling (figure 6(a)) and autolocalization (figure 6(b)) as has been used to describe the properties of  $DX^-$  centres. The potential curves  $U_1(x)$  and  $U_2(x)$  correspond to the electron bound to the impurity and to the ionized impurity with zero kinetic energy of the electron respectively. The equilibrium position of the bound state is shifted with respect to the ionized state due to the electron–phonon interaction. The energy separation between the two potentials is determined by the electron binding energy  $\varepsilon_b(x)$  as a function of the configuration coordinate  $x$ :

$$U_1(x) = U_2(x) - \varepsilon_b(x). \quad (1)$$

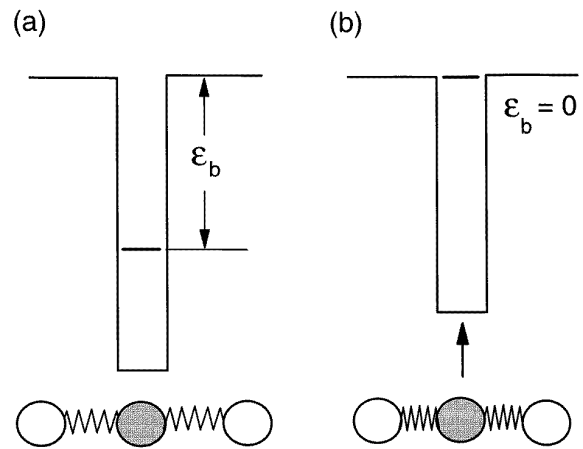


**Figure 5.** Schematic representation of the impurity binding energy  $\varepsilon_b$  as a function of atomic elongations: (a) ground state, (b) electron merging into the continuum.

The bound state equilibrium energy yields the value of the threshold of optical ionization:  $\varepsilon_b = \varepsilon_b(x = x_0) = \varepsilon_{opt}$ . Assuming the simple parabolic approach for  $U_1$ , as shown in figure 6,  $\varepsilon_{opt}$  is larger than the energy of thermal ionization  $\varepsilon_T$ . The relaxation energy  $\Delta\varepsilon = \varepsilon_{opt} - \varepsilon_T$  characterizes the strength of the electron–phonon coupling. The larger the magnitude of the coupling the larger is  $\Delta\varepsilon$ .

The configuration of figure 6(a) corresponds to on-site impurities. In this case the difference between  $\varepsilon_{opt}$  and  $\varepsilon_T$  is usually small. In fact for deep impurities in Ge no difference between  $\varepsilon_{opt}$  and  $\varepsilon_T$  has been observed as yet. There are, however, some cases where the relaxation energy  $\Delta\varepsilon$  is very large, as shown by Henry and Lang [21] for ‘state 2’ oxygen in GaP. The large value of  $\Delta\varepsilon$  has been attributed to two different vibrational frequencies for the occupied and unoccupied states respectively.

The configuration of figure 6(b) is usually assumed to apply to  $DX^-$  centres, giving the observed big difference between the optical ionization threshold  $\varepsilon_{opt}$  and the thermal ionization energy  $\varepsilon_T$  [1–5]. This difference is introduced by a large change in configuration coordinate between the ground state and the ionized configuration with little or no change in the vibrational frequency. This explains persistent photoconductivity since there is no optical relaxation pathway and there is a big potential barrier preventing excited electrons returning to the ground state. The details of the adiabatic potential configuration are of great importance for the non-radiative capture of free carriers.

The theory of carrier emission in static electric fields has been developed by Karpus and Perel [22], who analytically calculated the emission probability as a function of the field strength. In this work the Huang–Rhys model [23] has been considered for on-site impurities where the vibrational frequencies of both the ground state and the ionized state potentials are the same. We do not want to reproduce here this theory and in particular the general relation between the emission rate and the field strength, though we will use this formula to fit our experimental result in the transition regime from low to

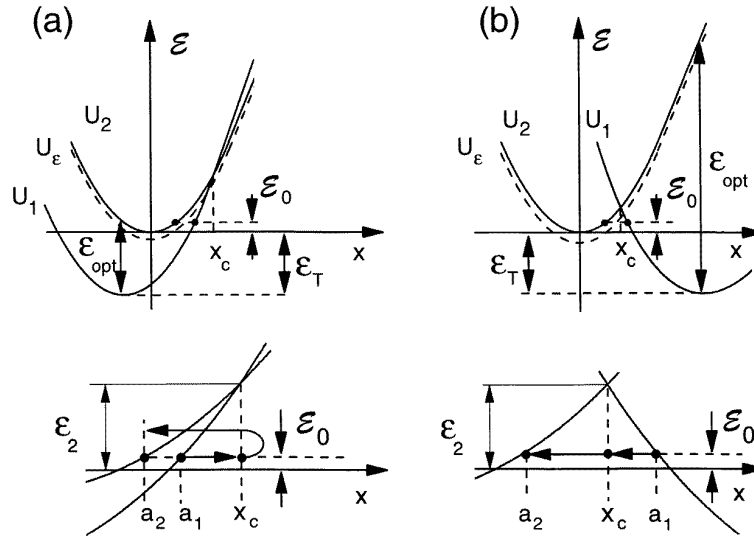


**Figure 6.** Upper panels: adiabatic potentials as a function of the configuration coordinate  $x$  of impurity motion for two possible schemes, (a) with and (b) without autolocalization.  $\mathcal{E}_T$  and  $\mathcal{E}_{opt}$  are thermal and optical activation energies respectively. Solid curves  $U_1$  and  $U_2$  correspond to the carrier bound to the centre and detached from the impurity at the bottom of the band ( $\mathcal{E} = 0$ ) respectively. The dashed curves are the potentials of an ionized impurity in an electric field. Lower panels: enlarged representations of the tunnelling trajectories.

high fields. Instead we will discuss approximate relations taking into account the limiting cases of small and high field strengths. Small fields are of particular importance for the present investigation because in this limit tunnelling times may be measured which allow us to distinguish between on-site and autolocalized impurity configurations. Finally, we will extend the discussion to charged impurities where the Coulomb potential causes a low-field correction to the emission rate due to the Poole–Frenkel effect [24].

### 3.2. Multiphonon thermal emission

We will first consider the zero-field thermal emission of carriers out of deep impurities in equilibrium where the emission is balanced by free carrier capture. For the sake of simplicity and to be specific we will discuss electrons, though the majority of the measurements have been carried out on acceptors in Ge. The following model of carrier emission applies equally well to electrons and holes.

In a classical approach the thermal emission rate is

$$e \propto \exp[-(\varepsilon_T + \varepsilon_2)/kT] \quad (2)$$

where  $\varepsilon_2 = U_1(x_c)$ ,  $x_c$  being the coordinate of intersection of  $U_1(x)$  and  $U_2(x)$  at which the electron binding energy  $\varepsilon_b(x)$  vanishes:  $\varepsilon_b(x_c) = 0$  (see figure 6). Thus,  $\varepsilon_T + \varepsilon_2$  is the minimum excitation energy necessary to drive the electrons into the continuum. Adopting the Huang–Rhys model, in which the adiabatic potential curves  $U_1(x)$  and  $U_2(x)$  are two identical displaced parabolas [23],  $\varepsilon_2 = (\varepsilon_T - \Delta\varepsilon)^2/4\Delta\varepsilon$ . Equation (2) with the large activation energy  $\varepsilon_T + \varepsilon_2$  holds only for high temperatures and it is practically never observed for weak coupling where  $\varepsilon_2 \gg \varepsilon_T$ . In this case and at low temperatures the observed activation energy is much smaller. Emission of the electron takes place at a vibrational energy  $\mathcal{E} < \varepsilon_2$

due to defect tunnelling from the bound configuration to the ionized configuration (see figure 6). With rising vibrational energy  $\mathcal{E}$ , the tunnelling barrier separating the potentials  $U_1$  and  $U_2$  at  $x < x_c$  decreases and hence the tunnelling probability increases. On the other hand the thermal population of a level at  $\mathcal{E}$  decreases with increasing  $\mathcal{E}$  as  $\exp(-\mathcal{E}/kT)$ . Thus, for each temperature an optimum energy  $\mathcal{E} = \mathcal{E}_0$  exists where the probability for tunnelling assumes a maximum (see [5, 20, 22]).

The defect tunnelling process will be treated in the semi-classical approximation. In this approach a particle has a well defined trajectory even below a potential barrier where the kinetic energy is negative. The thermal emission rate of a defect with vibrational energy  $\mathcal{E}$  at temperature  $T$  is now given by

$$P(\mathcal{E}) \propto \exp(-\psi) \quad (3)$$

with

$$\psi(\mathcal{E}) = (\varepsilon_T + \mathcal{E})/k_B T + 2|S(\mathcal{E})| \quad (4)$$

where  $S(\mathcal{E})$  is the principal function multiplied by  $i/\hbar$  [25]. The first term in equation (4) gives the thermal population of an energy level  $\mathcal{E}$  whereas the second term determines tunnelling from the bound to the ionized configuration. Due to the exponential dependence of  $P(\mathcal{E})$  on the energy  $\mathcal{E}$ , tunnelling takes place in a narrow range of  $\mathcal{E}$  around  $\mathcal{E}_0$  where  $\psi(\mathcal{E})$  assumes a minimum, i.e.  $d\psi/d\mathcal{E} = 0$ . The optimum tunnelling energy  $\mathcal{E}_0$  is obtained from the condition that the exponent of the emission probability  $\psi$  assumes a minimum at  $\mathcal{E} = \mathcal{E}_0$

$$\left. \frac{d\psi}{d\mathcal{E}} \right|_{\mathcal{E}=\mathcal{E}_0} = 2 \left. \frac{d|S(\mathcal{E})|}{d\mathcal{E}} \right|_{\mathcal{E}=\mathcal{E}_0} + \frac{1}{kT} = 0. \quad (5)$$

The magnitude of the derivative  $d|S|/d\mathcal{E}$  may be identified with the barrier tunnelling time  $\tau$  divided by  $\hbar$  [26].

Thus, in the case of phonon-assisted tunnelling we get  $\tau = \hbar/2kT$ .

After [22, 25]  $S(\mathcal{E})$  may be split into two parts,  $S(\mathcal{E}) = -S_1(\mathcal{E}) + S_2(\mathcal{E})$ , with

$$S_i(\mathcal{E}) = \frac{\sqrt{2M}}{\hbar} \int_{a_i}^{x_c} dx \sqrt{U_i(x) - \mathcal{E}} \quad i = 1, 2 \quad (6)$$

which correspond to two tunnelling trajectories, one from  $a_1$  to  $x_c$  under the potential  $U_1$  and the other from  $a_2$  to  $x_c$  under  $U_2$ . The real orientation of the tunnelling path along the coordinate  $x$  is introduced by the sign in front of  $S_i$ . In figure 6 the tunnelling trajectories for both impurity configurations are indicated by arrows.  $M$  in equation (6) is the effective mass of the local impurity vibrational mode. The essential difference with respect to tunnelling between the two configuration potential schemes in figures 6(a) and 6(b) is that  $S_1(\mathcal{E})$  and  $S_2(\mathcal{E})$  have the same signs for the on-site configuration (figure 6(a)) but the sign is opposite for autolocalization (figure 6(b)). Thus we have  $|S| = |S_2| - |S_1|$  for the on-site configuration and  $|S| = |S_1| + |S_2|$  for autolocalization, taking into account that  $|S_2| > |S_1|$  (see figure 6). The tunnelling times  $\tau_1$  and  $\tau_2$  along the trajectories under the corresponding potentials are

$$\begin{aligned} \tau_i &= \hbar \left. \frac{d|S_i|}{d\mathcal{E}} \right|_{\mathcal{E}=\mathcal{E}_0} \\ &= \sqrt{\frac{M}{2}} \left| \int_{a_i}^{x_c} \frac{dx}{\sqrt{U_i(x) - \mathcal{E}_0}} \right| \quad i = 1, 2. \end{aligned} \quad (7)$$

From equations (5) and (7) we find

$$\tau = \tau_2 \pm \tau_1 = \frac{\hbar}{2kT} \quad (8)$$

where the minus and plus signs correspond to figures 1(a) and (b) respectively. As  $\mathcal{E}_0$  is much larger than the minimum of  $U_1$ ,  $\tau_1$  is of the order of the period of oscillation in  $U_1$  and does not significantly depend on temperature and electric field. For on-site deep impurities such as Au, Hg, Zn, Cu in Ge it has been shown that  $\tau_2$  is larger than  $\hbar/2kT$  and follows the temperature dependence of equation (8) [5, 22]. For autolocalized states  $\tau_2$  is smaller than  $\hbar/2kT$  [5]. Thus, by measuring  $\tau_2$  a clear-cut distinction between on-site substitutional impurities and autolocalized configurations can be made.

In the case of weak electron–phonon coupling ( $\varepsilon_2 \gg \varepsilon_T$ ) one gets the simple relation for optimum defect tunnelling energy  $\mathcal{E}_0$ :

$$\mathcal{E}_0 = \varepsilon_T / [\exp(\hbar\omega/kT) - 1]. \quad (9)$$

For low temperatures,  $kT < \hbar\omega$  and  $\mathcal{E}_0 \ll \varepsilon_T$  one can assume  $\mathcal{E}_0 = 0$  in (7) when calculating  $\tau_1$  and find

$$\tau_1 = \sqrt{\frac{M}{2}} \int_{a_1}^{x_c} \frac{dx}{\sqrt{U_1(x)}} \quad (10)$$

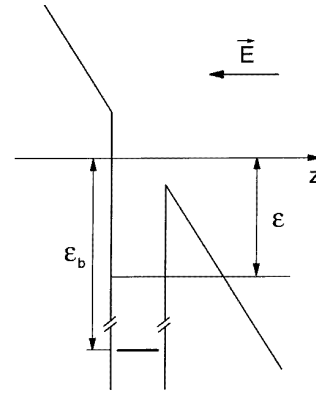


**Figure 7.** Electron potential barrier in an electric field directed along the  $z$  axis.  $\varepsilon_b$  is the binding energy and  $\varepsilon$  is the energy of the ejected electron.

which is independent of temperature. In the model of a parabolic potential  $U_1(x)$  with the vibrational frequency  $\omega$  the tunnelling time  $\tau_1$  is given for on-site impurities by

$$\tau_1 = \frac{1}{2\omega} \ln \frac{\varepsilon_T}{\varepsilon_{opt} - \varepsilon_T} \quad (11)$$

and in the case of autolocalization by

$$\tau_1 = \frac{1}{2\omega} \ln \frac{\varepsilon_{opt} - \varepsilon_T}{\varepsilon_T}. \quad (12)$$

### 3.3. Phonon-assisted tunnel ionization in the presence of an electric field

In a homogeneous electric field a potential of constant slope along the direction of the field vector is superimposed on the potential well binding the electron. A triangular potential barrier is formed that the electron may cross by tunnelling (see figure 7). This tunnelling process is different from the defect tunnelling discussed in the above section where the impurity configuration tunnels at constant energy from the adiabatic potential  $U_1$  to  $U_2$ . The electron may now be ejected into the continuum at negative electron energy  $\varepsilon$ . Defect tunnelling takes place in an ionized configuration  $U_\varepsilon = U_2 - \varepsilon$  which is shifted to lower energy by  $\varepsilon$  (broken curve in figure 6). We will consider here the limit of small electric field strengths where  $\varepsilon$  is small. Quantitatively  $\varepsilon$  should be smaller than  $\mathcal{E}_0$ . In this case the optimum energy  $\mathcal{E}_0$  of defect tunnelling remains unchanged. Then we get a first-order correction in  $\varepsilon$  of the exponent  $\psi$  of the emission probability determined in equation (3):

$$\psi(\mathcal{E}_0, \varepsilon) = \psi \Big|_{\varepsilon=0} + 2 \left. \frac{d|S_\varepsilon|}{d\varepsilon} \right|_{\varepsilon=0} \varepsilon \quad (13)$$

where

$$S_\varepsilon = \frac{\sqrt{2M}}{\hbar} \int_{a_2}^{x_c} dx \sqrt{U_2(x) - \varepsilon - \mathcal{E}_0}. \quad (14)$$

Then, the probability of thermal emission of a carrier with energy  $-\varepsilon$  is given by

$$e(\varepsilon) = e_0 \exp(2\varepsilon\tau_2/\hbar) \quad (15)$$

where  $\tau_2$  is the tunnelling time after equation (8) and  $e_0$  is the emission rate in the absence of an electric field. The emission rate of an electron with energy  $\varepsilon$  increases by the factor  $\exp(2|\varepsilon|\tau_2/\hbar)$ , because the defect tunnelling trajectory from  $x_c$  to the crossing point of  $U_\varepsilon$  with the vibrational energy level  $\mathcal{E}_0$  gets shorter.

The probability of electron tunnelling through the triangular barrier of height  $\varepsilon$  [25] (see figure 7) is proportional to  $\exp(-\frac{4}{3}\varepsilon^{3/2}\sqrt{2m^*}/\hbar eE)$  where  $E$  is the electric field strength and  $m^*$  the effective mass of the electron. In this way, the probability of the tunnelling emission, assisted by multiphonon transitions, as a function of  $\varepsilon$  is given by the product of rising and falling exponential functions:

$$e(E, \varepsilon) \propto \exp(2\varepsilon\tau_2/\hbar) \exp\left(-\frac{4}{3}\frac{\varepsilon^{3/2}\sqrt{2m^*}}{\hbar eE}\right). \quad (16)$$

Again, because of the exponential dependence of  $e(E, \varepsilon)$  on  $\varepsilon$ , the emission rate is determined by the maximum of the total exponent in equation (16), which corresponds to an electron energy

$$\varepsilon_m = \frac{\tau_2 e^2 E^2}{2m^*}. \quad (17)$$

Introducing this in equation (16) we get for the phonon-assisted tunnelling probability as a function of the electric field

$$e(E) = e_0 \exp\left(\frac{E^2}{E_c^2}\right) = e_0 \exp\left(\frac{\tau_2^3 e^2 E^2}{3m^*\hbar}\right) \quad (18)$$

where  $e_0$  is the multiphonon ionization probability in thermal equilibrium. The emission rate in an electric field increases by factor  $\exp(E^2/E_c^2)$  where  $E_c^2 = 3m^*\hbar/\tau_2^3 e^2$  is a characteristic field strength determined by the tunnelling time  $\tau_2$  and, thus, is temperature dependent. The slope of the exponent in equation (18) as a function of  $E^2$  rises with falling temperature. The ratio  $e(E)/e_0$  of the emission rate at an electric field  $E$  is larger for smaller temperatures. This is caused by the fact that at low temperatures the thermal electron emission in equilibrium  $e_0$  vanishes because the vibrational tunnelling energy  $\mathcal{E}_0$  approaches zero and the tunnelling time  $\tau_2$  goes to infinity. Hence a small drop of adiabatic potential  $U_2$  of the ionized impurity leads to a large increase of the emission probability. These temperature and electric field dependences of carrier emission probability have been observed in d.c. fields [27, 28].

### 3.4. Direct electron tunnel ionization

The emission rate as a function of the electric field in equation (18) has been obtained with the assumption that electron tunnelling produces small corrections to multiphonon emission in equilibrium. That means that the electron tunnelling energy  $\varepsilon_m$  is much smaller than the vibrational tunnelling energy of the defect  $\mathcal{E}_0$  and the thermal energy  $\varepsilon_T$ . These conditions set an upper limit to the electric field

$$E \ll E_0/2\omega\tau_2 \quad (19)$$

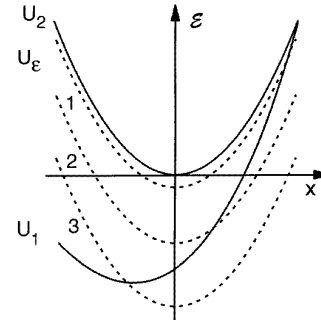


**Figure 8.** Schematic representation of the adiabatic potentials as functions of a configuration coordinate of impurity motion. Solid curves  $U_1$  and  $U_2$  correspond to the electron bound to the centre and detached from the impurity at the bottom of the valence band ( $\varepsilon = 0$ ) respectively. The dashed curves are the potential of the ionized impurity for different electric field strengths: (1) phonon-assisted tunnelling; (2) intermediate case; (3) direct electron tunnelling.

where

$$E_0 = \frac{2\omega\sqrt{2m^*\varepsilon_T}}{e}. \quad (20)$$

In the opposite limit  $E \gg E_0$ , direct tunnelling of carriers from bound states to the continuum without involving thermal phonons occurs and dominates the ionization of impurities. The adiabatic potential of the ionized defect for various field strengths is shown in figure 8. At low temperatures direct electron tunnelling takes place at the crossing point of this potential curve and  $U_1$ . The tunnelling probability is given by the transmission of the electron through the triangular potential barrier of the electron potential [22] which has already been used in equation (16)

$$e(E) = \frac{eE}{2\sqrt{2m\varepsilon_{opt}}} \exp(-\phi) \quad (21)$$

where

$$\phi = \frac{4}{3}\frac{\varepsilon^{3/2}\sqrt{2m^*}}{\hbar eE}. \quad (22)$$

The tunnelling energy of the electron is  $\varepsilon = \varepsilon_{opt}$  if the  $U_\varepsilon$  crosses the bound state potential  $U_1$  at its minimum. If this is not the case but the crossing is still close to the minimum, phonon-assisted tunnelling yields a small temperature-dependent correction additive to  $\phi$  which is unimportant at high electric field strengths [22]. Equations (21) and (22) show that the emission rate for direct tunnelling depends less strongly on the electric field strength than phonon-assisted tunnelling (equation (18)).

### 3.5. Coulomb charge effect

The deep acceptors in Ge investigated here are singly charged impurities. Thus the long-range Coulomb potential must be taken into account in addition to the deep well causing the large binding energy of the carrier. For a Coulomb potential, in contrast to a potential well, the height of an energy barrier formed by an external electric field is lowered along the direction of the electric field vector.

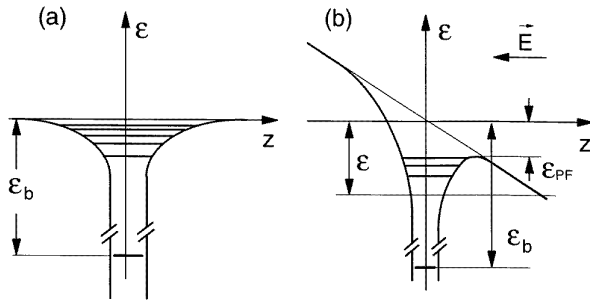


**Figure 9.** Potential of a charged deep impurity in the absence (a) and presence (b) of an electric field  $E$  applied along axis  $z$ .  $\varepsilon_b$  is the ground state binding energy and  $\varepsilon_{PF}$  is the Poole–Frenkel reduction of the potential barrier height.

Therefore an electric field yields an increase of the thermal emission probability by excitation of a carrier across the barrier, without tunnelling. The theory of this electric-field-assisted ionization was developed by Frenkel [24] and Onsager [29] and is usually called the Poole–Frenkel effect. The current flow in the sample increases exponentially with the square root of the applied electric field. The Poole–Frenkel effect is the dominant mechanism of electric-field-assisted thermal ionization at not too high field strengths before tunnelling of carriers becomes important [5]. It has been observed in the current–voltage characteristics under d.c. conditions in many insulators and semiconductors.

A simple calculation shows that in an electric field  $E$  the ionization barrier is diminished (see figure 9) by an amount  $\varepsilon_{PF}$ , given by

$$\varepsilon_{PF} = 2\sqrt{\frac{Ze^3E}{\kappa}} \quad (23)$$

where  $Z$  is the charge of the centre and  $\kappa$  is the dielectric constant.

Owing to this fact, the probability of thermal emission due to an electric field increases as

$$e(E) \propto \exp(\varepsilon_{PF}/kT). \quad (24)$$

In semiconductors this effect is observed for attractive Coulomb impurity centres at high temperatures and electric field strengths  $E$ , being less than the field which yields  $\varepsilon_{PF}(E) = Z^2Ry^*$ , where  $Ry^*$  is the effective Rydberg energy of the electron in the Coulomb potential of the charged impurity.

An analytical relation for the emission probability cannot be given for low electric field strengths if the electron tunnelling energy  $\varepsilon_m$  is smaller than the Rydberg energy. If tunnelling occurs, at higher fields, the role of a charge is reduced to increase the barrier transparency because of the lowering of the barrier height. This gives only a correction to the tunnel ionization probability. This correction has been calculated in [30] in the limit  $\varepsilon_m > Ry^*$ , yielding multiplicative factors for the emission rate  $e(E)$  of equation (18):

$$e(E) = e_0 \exp \left[ \frac{2\sqrt{2m^*Ry^*}}{eE\tau_2} \ln \left( \frac{4\tau_2^3 e^2 E^2}{m^*\hbar} \right) \right]$$

$$\times \exp \left( \frac{\tau_2^3 e^2 E^2}{3m^*\hbar} \right). \quad (25)$$

Thus, taking into account the Poole–Frenkel effect and multiphonon tunnelling ionization with the charge correction given in the above equation, we find that the logarithm of  $e(E)$  varies as a function of the electric field first like  $\sqrt{E}$  and then changes to an  $E^2$  dependence for high fields. The correction due to the charge in equation (25) approaches unity for increasing  $E$  and therefore the charge correction becomes unimportant at high fields.

### 3.6. The electric field of far-infrared radiation

It has been shown by Keldysh [16] that multiphoton ionization and tunnelling ionization in high-frequency radiation fields are two limiting cases of just the same nonlinear optical process. Application of a quantum mechanical or classical picture of the electromagnetic field depends on the magnitude of the radiation frequency  $\Omega$ . The radiation may be assumed to be a classical field if  $\Omega$  is smaller than the characteristic frequencies of the atomic system under consideration.

In the present case of phonon-assisted tunnelling ionization of deep impurities, the results developed in the previous sections for static electric fields may be applied if the radiation frequency  $\Omega$  is less than the frequency of the defect vibrational mode,  $\omega$ , which is of the order of the optical phonon frequency. A further condition is that the time of defect tunnelling under the adiabatic configuration potential should be less than the period  $\Omega^{-1}$  of the radiation field. The emission probability depends on the instantaneous magnitude of the electric field strength. As the electric field appears in the argument of an exponential function, carrier emission is determined by the amplitude of the electric field strength of the radiation.

If the radiation frequency is of the same order or larger than the characteristic frequency of the atomic system, the quantum picture of the electromagnetic field must be considered. This yields a frequency-dependent emission ionization probability [16].

## 4. Experimental results and discussion

The investigations of different materials with deep impurities such as Ge doped by Au, Hg, Zn, Cu and  $Al_xGa_{1-x}Sb$  have shown a photoconductive signal depending exponentially on the square of the electric field strength of the radiation. This behaviour, which is characteristic for phonon-assisted tunnelling, has been observed for all samples in a wide range of field strengths and temperatures. The experimentally determined dependence of  $\ln(\sigma_i/\sigma_d)$  on the square of the amplitude of the optical electric field is shown for Ge(Au) (doping density  $7 \times 10^{14} \text{ cm}^{-3}$ ) in figure 10 and for  $Al_xGa_{1-x}Sb$  in figure 11. In both figures measurements are plotted for different temperatures obtained at the wavelengths  $\lambda = 90.5 \mu\text{m}$  and  $250 \mu\text{m}$ . It is seen that there is a range of field strength for each temperature where the probability

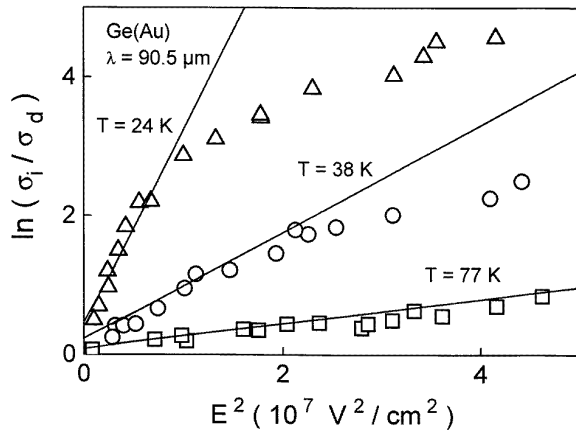


**Figure 10.** Dependence of  $\ln(\sigma_i/\sigma_d)$  for Ge(Au) ( $E_i \sim 150$  meV) at three different temperatures on the square of the strength of the optical electric field,  $E^2$ , at wavelength  $\lambda = 90.5$   $\mu\text{m}$  ( $\hbar\omega = 13.7$  meV). Lines are fitted to the linear range of the data by  $\sigma_i/\sigma_d \propto \exp(E^2/E_c^2)$ .

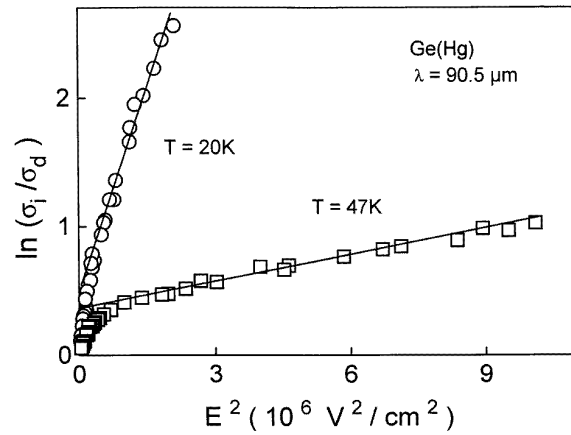


**Figure 12.** Dependence of  $\ln(\sigma_i/\sigma_d)$  for Ge(Hg) (binding energy  $E_i \sim 90$  meV) as a function of the square of the strength of the optical electric field,  $E^2$ .  $\lambda = 90.5$   $\mu\text{m}$  (photon energy 13.7 meV),  $T = 47$  K and 20 K.

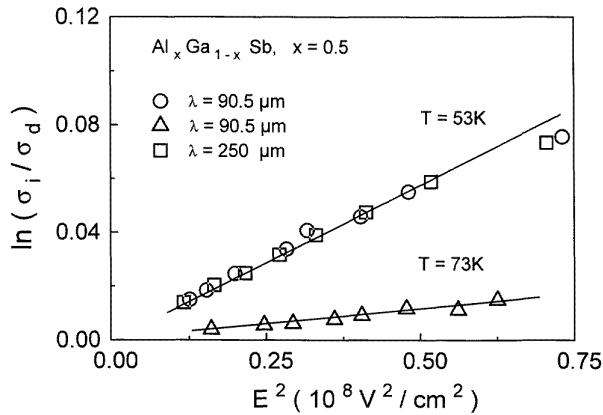


**Figure 11.** Dependence of  $\ln(\sigma_i/\sigma_d)$  for  $\text{DX}^-$  centres in  $\text{Al}_x\text{Ga}_{1-x}\text{Sb}$ ,  $x = 0.5$ , on the square of the strength of the electric field of the radiation at different temperatures and wavelengths. Lines are fitted to the linear range of the data by  $\sigma_i/\sigma_d \propto \exp(E^2/E_c^2)$ .

of photoexcitation depends on the electric field amplitude like  $\exp(E^2/E_c^2)$ .

In figures 10 and 11, fittings of the experimental data by the relation  $\exp(E^2/E_c^2)$  are drawn by full lines. Extrapolating these lines to zero field strength shows that  $\ln(\sigma_i/\sigma_d)$  does not approach zero. This means that we do not obtain  $\sigma_i = \sigma_d$  for vanishing electric field strength as it must be and as it is expected from equation (18). Additionally the slope of the experimental curves change at high levels of the field. The measured ionization probability increases more slowly with rising electric field strength than given by  $\exp(E^2/E_c^2)$ .

We will first discuss the limit of low field strengths. This range is shown more clearly in figure 12 where the dependence of  $\ln(\sigma_i/\sigma_d)$  on  $E^2$  is displayed for Ge(Hg) (doping density  $4 \times 10^{14}$   $\text{cm}^{-3}$ ). This impurity has a smaller binding energy,  $\varepsilon_T = 90$  meV, in comparison with Ge(Au),  $\varepsilon_T = 150$  meV. The measurements demonstrate that  $\sigma_i$  in

fact equals  $\sigma_d$  at zero field but the emission probability does not depend exponentially on the square of the field strength. The deviation of the photoconductive signal from the  $\exp(E^2/E_c^2)$  dependence is due to the lowering of the tunnelling barrier caused by the charge of the impurities. As long as the drop of the observed signal below the extrapolated  $\exp(E^2/E_c^2)$  curve is small, the ionization probability may be described by the charge correction to phonon-assisted tunnelling introduced in equation (25). At even lower field strengths the Poole–Frenkel effect overrides phonon-assisted tunnelling and dominates the emission of carriers. This is demonstrated in figure 13 where  $\ln(\sigma_i/\sigma_d)$  is plotted as a function of the *square root*,  $\sqrt{E}$ , of the electric field amplitude of the high-frequency radiation. The full lines are fits which show that the probability of ionization may well be described by the relation  $e(E) \propto \exp\sqrt{E/E_{PF}}$  for small field strengths. The ionization probability strongly rises with decreasing temperature. The  $\sqrt{E}$  dependence of  $\ln(\sigma_i/\sigma_d)$  and the temperature variation are in good agreement with equations (23) and (24) of the Poole–Frenkel effect. The simple theory yielding these equations, however, does not give a full account of the conductivity  $\sigma_i$  as a function of the high-frequency electric field. The discrepancies are exactly the same as observed in the case of d.c. electric fields [31, 32]. The slope of  $\ln(\sigma_i/\sigma_d)$  is only about one half of that predicted by equations (23) and (24) and the photoconductivity saturates at low fields [31–34]. These features of the photoconductivity at terahertz frequencies are in excellent agreement with published data of the enhanced conductivity of semiconductors in d.c. electric fields. They are also well described by more realistic theoretical approaches which consider the emission of carriers in three dimensions and in some cases take into account carrier distribution statistics [34] or are based on the Onsager theory of dissociation [33, 34]. These experimental and theoretical results additionally confirm our conclusion that the observed photoconductive signal at photon energies much less than the binding energy of the deep acceptors is due to the electric field of the high-frequency radiation.

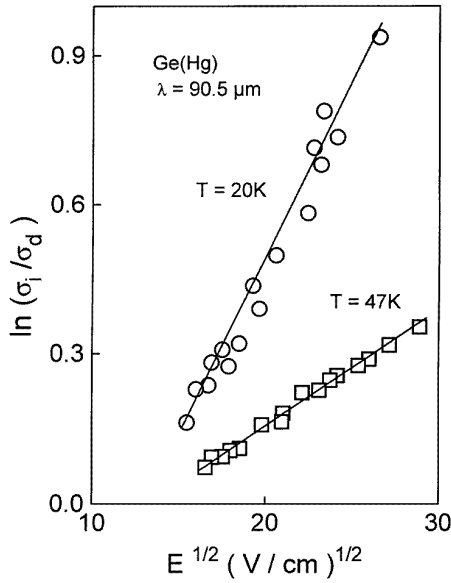


**Figure 13.** Dependence of  $\ln(\sigma_i/\sigma_d)$  on the square root of the strength of the optical electric field,  $\sqrt{E}$ , at wavelengths  $\lambda = 90.5 \mu\text{m}$  (13.7 meV) for  $T = 47 \text{ K}$  and  $20 \text{ K}$  for Ge(Hg) ( $E_i \sim 90 \text{ meV}$ ).

We will now come back to phonon-assisted tunnelling. As seen from equation (17), the slope of the experimental curves in the field range where  $\ln(\sigma_i/\sigma_d) \propto \exp(E^2/E_c^2)$  permits us to determine the value of the tunnelling time  $\tau_2$ . In order to calculate  $\tau_2$  from experimental data it is necessary to know what kind of effective carrier mass is involved for acceptors in Ge. In figure 14 tunnelling times  $\tau_2$  as functions of reciprocal temperature are plotted for all investigated deep impurities. In the case of deep acceptors the light-hole mass has been used for evaluation. Figure 14 shows that for both types of impurities  $\tau_2$  follows equation (8) in very good agreement. Using the heavy-hole mass, a constant slope of  $\tau_2$  as a function of  $1/T$  cannot be achieved. This result allows us to conclude that carriers bound to deep acceptors in Ge will predominantly tunnel into the light-hole band. The site symmetry of substitutional impurities is the point group  $T_d$ . The ground state of the deep impurity represents an admixture of light and heavy holes. Thus, neither the light- nor the heavy-hole mass may be attributed to a hole bound to an acceptor. For the tunnelling process, however, the tail of the wavefunction far from the centre is important. As shown in a theoretical work on tunnelling [35], light holes contribute most to the wavefunction tail.

For the purpose of comparison,  $\hbar/2kT$  is also plotted in figure 14 and shows that  $\tau_2$  is of the order of magnitude of  $\hbar/2kT$ . However, as an important result the experimental data in figure 14 demonstrate that for any temperature  $\tau_2$  is larger than  $\hbar/2kT$  for an on-site impurity whereas it is smaller than  $\hbar/2kT$  for the autolocalized  $\text{DX}^-$  centres. This observation is in excellent agreement with equation (8). Thus, on-site impurities and autolocalized centres may be unambiguously distinguished by phonon-assisted tunnelling induced by terahertz frequency radiation. The temperature-independent tunnelling times  $\tau_1 = |\tau_2 - \hbar/2kT|$  are given

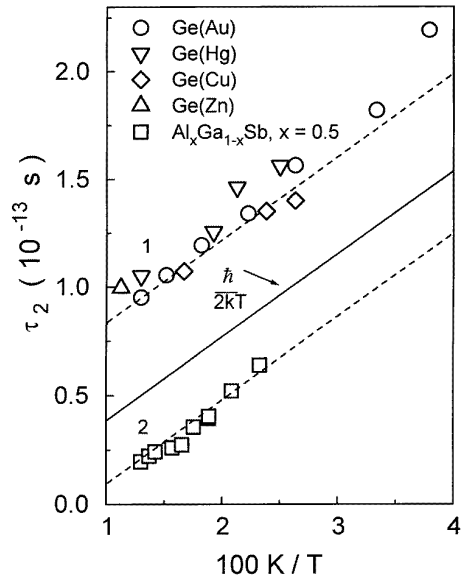


**Figure 14.** Tunnelling time  $\tau_2$  calculated from the experimental characteristic fields  $E_c$  as a function of inverse temperature:  $\circ$ , Ge(Au);  $\nabla$ , Ge(Hg);  $\diamond$ , Ge(Cu);  $\triangle$ , Ge(Zn);  $\square$ ,  $\text{DX}^-$  centres in  $\text{Al}_x\text{Ga}_{1-x}\text{Sb}$ ,  $x = 0.5$ . Broken line 1 shows  $\tau_2 = \hbar/2kT + \tau_1$  with  $\tau_1 = 4.5 \times 10^{-14} \text{ s}$ . Broken line 2 shows  $\tau_2 = \hbar/2kT - \tau_1$  with  $\tau_1 = 2.9 \times 10^{-14} \text{ s}$ .

in the caption of figure 14. Within the accuracy of the measurement,  $\tau_1$  is the same for all investigated deep impurities in Ge and of the same order for  $\text{DX}^-$  centres.

Finally we will consider the high electric field range. The observed photoconductive signals drop above a characteristic field strength  $E^*$  below that of phonon-assisted tunnelling extrapolated to high fields. This is shown in figures 15–17 where  $\ln(\sigma_i/\sigma_d)$  is plotted as a function of the square of the amplitude of the electric field  $E$  for Ge(Au) and Ge(Hg) at different wavelengths and various temperatures. For fields strengths  $E$  larger than  $E^*$  the ionization probability increases more slowly with rising  $E$  than in the range of phonon-assisted tunnelling.

It was shown in section 3 that phonon-assisted tunnelling in the electric field represents a small correction to multiphonon thermal emission. The emission probability is proportional to  $\exp(E^2/E_c^2)$  and has been derived with the assumption that the electron tunnelling energy  $\varepsilon_m$  (equation (16)) is less than the defect tunnelling energy  $\mathcal{E}_0$  (equation (9)). With increasing electric field strength the electron tunnelling energy also increases and  $\mathcal{E}_0$  drops. The phonon-assisted tunnelling approximation breaks down if  $\varepsilon_m$  becomes equal to  $\mathcal{E}_0$ . Thus we may identify  $E^*$  with the electric field at which  $\varepsilon_m = \mathcal{E}_0$ , yielding

$$E^{*2} = \frac{2\varepsilon_T k T m^*}{\hbar \omega e^2 \tau_2}. \quad (26)$$

At higher electric field strengths carrier emission is achieved by direct tunnelling [7].

In the theory of Karpus and Perel [22] the emission probability in the electric field range from phonon-assisted tunnelling to direct tunnelling is determined by three phenomenological parameters, namely the thermal binding

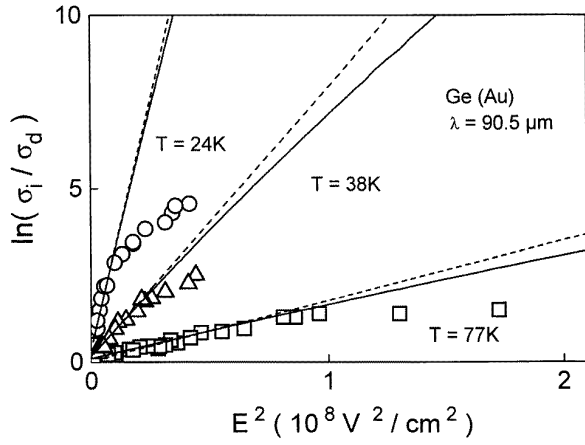


**Figure 15.** Dependence of  $\ln(\sigma_i/\sigma_d)$  on the square of the strength of the optical electric field,  $E^2$ , for Ge(Au) ( $E_i \sim 150$  meV) at three different temperatures. Broken lines are calculated after  $\sigma_i/\sigma_d \propto \exp(E^2/E_c^2)$  with  $\tau_2$  taken from the experiment. Full lines are calculated after the Karpus–Perel theory (equations (25) and (26) in [22]) using the same  $\tau_2$  and  $\omega = 3 \times 10^{13} \text{ s}^{-1}$ .

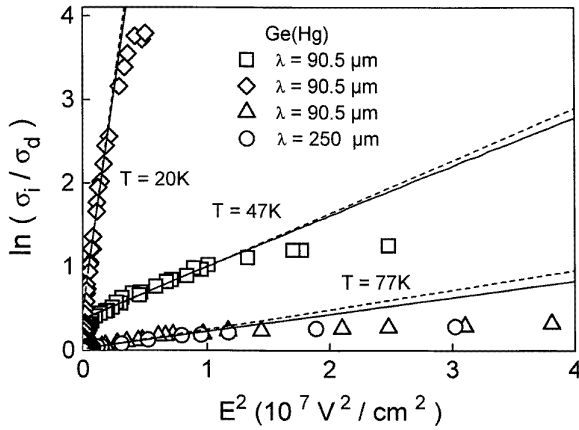


**Figure 16.** Dependence of  $\ln(\sigma_i/\sigma_d)$  on the square of the strength of the optical electric field,  $E^2$ , for Ge(Hg) ( $E_i \sim 90$  meV) at three different temperatures. Broken lines are calculated using  $\sigma_i/\sigma_d \propto \exp(E^2/E_c^2)$  with  $\tau_2$  taken from the experiment. Full lines are calculated after the Karpus–Perel theory (equations (25) and (26) in [22]) using the same  $\tau_2$  and  $\omega = 3 \times 10^{13} \text{ s}^{-1}$ .

energy  $\varepsilon_T$ , the frequency of the local impurity vibrational mode  $\omega$ , and the dimensionless constant of electron–phonon coupling  $\beta = \Delta\varepsilon/\varepsilon_T$ . The parameter  $\beta$  is related to  $\tau_1$  by equation (11). Taking  $\varepsilon_T$  from the literature and  $\tau_1$  from our measurements at  $E < E^*$ , we have calculated the probability of tunnelling ionization after the Karpus–Perel theory. The only free parameter was the frequency  $\omega$ , which was obtained by fitting the photoconductive signal at the electric field  $E^*$  for one temperature. This frequency has been used to calculate the emission probability for all temperatures and all impurities. No fitting parameter was used. Figure 18 shows calculations of the emission probability in the electric field  $e(E)$  normalized by the thermal emission probability  $e_0$  for different local vibration

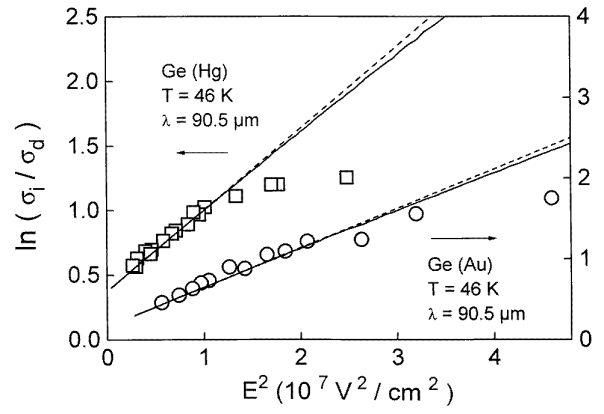


**Figure 17.** Dependence of  $\ln(\sigma_i/\sigma_d)$  on the square of the strength of the optical electric field,  $E^2$ , for  $\lambda = 90.5 \mu\text{m}$  ( $\hbar\omega = 13.7$  meV) and  $T = 46$  K, for Ge(Au) ( $E_i \sim 150$  meV) and Ge(Hg) ( $E_i \sim 90$  meV). Broken lines are calculated using  $\sigma_i/\sigma_d \propto \exp(E^2/E_c^2)$  with  $\tau_2$  taken from the experiment. Full lines are calculated using the Karpus–Perel theory (equations (25) and (26) in [22]) using the same  $\tau_2$  and  $\omega = 3 \times 10^{13} \text{ s}^{-1}$ . Note the different ordinate scales for Ge(Hg) and Ge(Au).

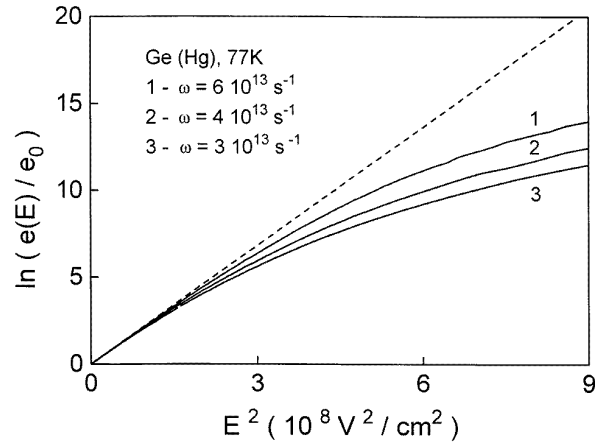


**Figure 18.** Dependence of  $\ln(e(E)/e_0)$  for Ge(Hg) ( $E_i \sim 90$  meV) at  $T = 77$  K. The broken line was calculated using  $\sigma_i/\sigma_d \propto \exp(E^2/E_c^2)$  with  $\tau_2$  taken from experiment. Curves 1 to 3 are calculated after the Karpus–Perel theory (equations (25) and (26) in [22]) using the same  $\tau_2$  and different frequencies  $\omega$  given in the figure.

frequencies  $\omega$ . The results demonstrate that the emission probability depends sensitively on  $\omega$  in the range of fields  $E > E^*$ . Thus it may be regarded as a reasonable fitting parameter.

Figures 15 to 17 present numerical calculations in comparison with experimental data. As a result we find that the theory fits the phonon-assisted tunnelling but does not reproduce the measured photoconductive signal for  $E > E^*$ . In this field range the calculated emission probability is, as expected, smaller than that of phonon-assisted tunnelling extrapolated to higher field strengths, but the experimental data are still below the calculated curves. The characteristic electric field  $E^*$  as a function of temperature and binding energy, however, is in good

agreement with the theory for all on-site impurities without additional fitting.

One reason for the discrepancy between theory and experiments at high electric fields could be phonon scattering of tunnelling carriers under the potential barrier, which sets an upper limit for the tunnelling probability. Such a process has been considered for the tunnelling of carriers through Schottky barriers [36] where the tunnelling probability has also been found to be smaller than theoretically predicted. With an increase of the electric field the value of the electron tunnelling energy  $\varepsilon_m$  and the length of tunnelling trajectory below the barrier increase so that scattering processes limit the emission rate.

## 5. Conclusion

In summary, photoionization of deep impurity centres in semiconductors has been investigated by high-power pulsed far-infrared laser light with quantum energies of the radiation much smaller than the impurity ionization energy. A photoconductive signal increasing nonlinearly with rising incident power has been observed for various deep on-site acceptors in Ge and autolocalized  $DX^-$  centres in  $Al_xGa_{1-x}Sb$ . As an important result, the signal strength at a given temperatures has been found to be independent of far-infrared radiation frequency, suggesting that the signal is caused by electric field ionization rather than multiphoton transitions. A detailed comparison of the experimental results with the theory of thermal and cold ionization of deep impurities in an electric field has shown that the field at terahertz frequencies acts like a d.c. field. Ionization of impurities takes place within one period of the field as long as the attractive impurity potential adiabatically follows the oscillation of the radiation field.

Over a substantial range of electric field strengths, the emission probability of carriers could be attributed to phonon-assisted tunnelling. The thermal emission of carriers from the impurity bound state into the continuum is usually accomplished by thermal activation of the system in the adiabatic bound state potential and tunnelling of the bound defect configuration into the ionized configuration. An electric field enhances defect tunnelling due to electron tunnelling through the barrier formed by the electron potential and the electric field. This increase in emission of carriers has been detected as a photoconductive signal. The electric field dependence of the observed signal allowed us to determine defect tunnelling times. It has been shown that, due to different tunnelling trajectories, on-site impurities and autolocalized centres may be unambiguously distinguished by the value of the tunnelling time compared to the reciprocal temperature multiplied by universal constants.

At relatively small and at very high electric field strengths the observed ionization probability deviates from that of phonon-assisted tunnelling. It has been shown that at low fields ionization of on-site impurities is caused by the Poole–Frenkel effect due to the charge of the defects. At high fields direct tunnelling in the electric field without thermal phonon activation occurs. The emission probability has been found to be smaller than

expected from theory. This observation has been tentatively attributed to scattering of tunnelling carriers by phonons, which limits the tunnelling rate at high fields. For a full understanding, further experimental investigations and theoretical considerations are needed.

The effect of an electric field on the thermal emission and capture of carriers is of importance for the kinetics and dynamics of semiconductors. High static electric fields drive the system into avalanche breakdown, which is usually associated with a large increase in noise, self-generated oscillations and current filamentations. These effects substantially change the properties of the material and disguise the elementary properties of tunnelling. The present method of ionizing impurities by short far-infrared laser pulses avoids these problems. The radiation pulse is shorter than the time needed to form a free carrier avalanche, and therefore extremely high electric field strengths may be applied. The d.c. bias field required to record photoconductivity may be kept well below the threshold of instability where the perturbation of the electron system is small, avoiding injection at the contacts. The intrinsically high sensitivity of photoconductivity gives a measurable signal from a few radiation-excited carriers.

## Acknowledgments

Financial support by the Deutsche Forschungsgemeinschaft is gratefully acknowledged. We thank V I Perel for helpful discussions.

## References

- [1] Mooney P M and Theis T N 1992 *Comments Condens. Matter Phys.* **16** 167
- [2] Newman R C 1994 *Semicond. Sci. Technol.* **9** 1749
- [3] Mooney P M 1990 *J. Appl. Phys.* **67** R1
- [4] Martin G M and Makram-Ebeid S 1986 *Deep Centers in Semiconductors* ed S T Pantelides (New York: Gordon and Breach)
- [5] Abakumov V N, Perel V I and Yassievich I N 1991 *Nonradiative Recombination in Semiconductors (Modern Problems in Condensed Matter Sciences 33)* ed V M Agranovich and A A Maradudin (Amsterdam: North-Holland)
- [6] Ganichev S D, Prettl W and Huggard P G 1993 *Phys. Rev. Lett.* **71** 3882
- [7] Ganichev S D, Diener J and Prettl W 1994 *Solid State Commun.* **92** 883
- [8] Ganichev S D, Diener J, Yassievich I N and Prettl W 1995 *Europhys. Lett.* **29** 315
- [9] Ganichev S D, Yassievich I N, Prettl W, Diener J, Meyer B K and Benz K W 1995 *Phys. Rev. Lett.* **75** 1590
- [10] Meyer B K, Bishopink G, Benz K W, Schöner A and Pensl G 1993 *J. Crystal Growth* **128** 475
- [11] Krause-Rehberg R, Drost Th, Polity A, Roos G, Pensl G, Volm D, Meyer B K, Bishopink G and Benz K W 1993 *Phys. Rev. B* **48** 11 723
- [12] Bishopink G 1992  $AlGa_{1-x}Sb_x$  Volumenkristalle aus schmelzflüssigen Lösungen *Dissertation* Universität Freiburg
- [13] Buryak E V, Kaufman S A and Kulikov K M 1963 *Fiz. Tverd. Tela* **5** 345 (Engl. Transl. 1963 *Sov. Phys.—Solid State* **5** 249)

- [14] Kaufman S A and Kulikov K M 1965 *Fiz. Tverd. Tela* **7** 3132 (Engl. Transl. 1966 *Sov. Phys.—Solid State* **7** 2536)
- [15] Rühle W, Jakowetz W and Pilkuhn M 1973 *Luminescence of Crystals, Molecules, and Solutions* ed F Williams (New York: Plenum) p 444
- [16] Keldysh L V 1964 *Zh. Eksp. Teor. Fiz.* **47** 1945 (Engl. Transl. 1965 *Sov. Phys.—JETP* **20** 1307)
- [17] Böhm W, Ettliger E and Prettl W 1981 *Phys. Rev. Lett.* **47** 1198
- [18] Guimaraes P S S, Keay B J, Kaminski J P, Allen S J, Hopkins P F, Gossard A C, Florez L T and Harbinson J P 1993 *Phys. Rev. Lett.* **70** 3792
- [19] Ganichev S D, Emel'yanov S A, Dmitriev A P, Terent'ev Ya V, Yaroshetskii I D and Yassievich I N 1986 *Zh. Eksp. Teor. Fiz.* **90** 445 (Engl. Transl. 1986 *Sov. Phys.—JETP* **63** 256)
- [20] Makram-Ebeid S and Lannoo M 1982 *Phys. Rev. B* **25** 6406
- [21] Henry C H and Lang D V 1977 *Phys. Rev. B* **15** 989
- [22] Karpus V and Perel V I 1986 *Zh. Eksp. Teor. Fiz.* **91** 2319 (Engl. Transl. 1986 *Sov. Phys.—JETP* **64** 1376)
- [23] Huang K and Rhys A 1950 *Proc. R. Soc. A* **204** 406
- [24] Frenkel J 1938 *Phys. Rev.* **54** 647
- [25] Landau L D and Lifshitz E M 1977 *Quantum Mechanics* (Oxford: Pergamon) p 185
- [26] Landauer R and Martin Th 1994 *Rev. Mod. Phys.* **66** 217
- [27] Tasch A F Jr and Sah C T 1970 *Phys. Rev. B* **1** 800
- [28] Irmischer K, Klose H and Maass K 1983 *Phys. Status Solidi a* **75** K25
- [29] Onsager L 1938 *Phys. Rev.* **54** 554
- [30] Abakumov V N, Perel V I and Yassievich I N 1988 *Fiz. Tekh. Poluprovodn.* **22** 262 (Engl. Transl. 1988 *Sov. Phys.—Semicond.* **22** 159)
- [31] Ieda M, Sawa G and Kato S 1971 *J. Appl. Phys.* **42** 3737
- [32] Hirai T and Nakada O 1968 *Japan. J. Appl. Phys.* **7** 112
- [33] Pai D 1975 *J. Appl. Phys.* **46** 5122
- [34] Connell G A N, Camphausen D L and Paul W 1972 *Phil. Mag.* **26** 541
- [35] Merkulov I A, Pakhomov A A and Yassievich I N 1986 *Fiz. Tverd. Tela* **28** 2127 (Engl. Transl. 1986 *Sov. Phys.—Solid State* **28** 1188)
- [36] Combescott R and Schreder G 1974 *J. Phys. C: Solid State Phys.* **7** 1318